Materials Horizons

ROYAL SOCIETY OF CHEMISTRY

COMMUNICATION

View Article Online
View Journal

Cite this: DOI: 10.1039/d5mh02462e

Received 28th December 2025,
Accepted 26th March 2026

DOI: 10.1039/d5mh02462e

rsc.li/materials-horizons

Frontal curing of aluminosilicate–epoxy composites for extreme underwater environments

Aolin Hou,[a] Ruochen Liu,[a] Jae Gwang Kim,[a] Prashant Dhakal,[b] Xiaofei Wu,[b] Jingjing Qiu*[c] and Shiren Wang *[ab]

Rapid underwater repair using durable materials capable of withstanding extreme cold and saline marine conditions remains a significant unresolved challenge with broad implications for the maintenance and restoration of marine infrastructure. In this work, we developed a new class of functional materials, aluminosilicate–epoxy composites with self-initiated, frontal curing and seawater resistance, to address this challenge. A catalyzed stoichiometric frontal polymerization strategy was employed to overcome the fundamental chemical incompatibility between the frontal curing of epoxy and the alkali-activated geopolymerization of aluminosilicate. Distinct from traditional external photo- or thermal stimuli, calcium oxide hydration was used to trigger frontal curing in seawater, thereby eliminating external energy input during both initiation and curing. The underwater front-cured aluminosilicate–epoxy composite exhibits a compressive strength of 48.3 MPa and an adhesive strength of 5.57 MPa on steel within one hour. The key property indicator (KPI), defined as the ratio of minimal operational compressive strength to the required curing time, outperforms state-of-the-art performance by 87.4-fold. Moreover, the composites exhibit high ultraviolet resistance (92% strength retention) and seawater resistance (96.25% strength retention with 0.26% mass loss) after 720 hours of UV exposure and 7 days of seawater immersion. The frontal curing of seawater-resistant hybrid materials represents a paradigm shift in underwater repair, with substantial potential to transform marine infrastructure restoration.

New concepts

Traditionally, underwater repairs demand substantial external power, hardware, and operational support, making deployment in off-grid, deep-water, or emergency scenarios logistically complex, costly, and often impractical. This work demonstrates a new concept for rapid underwater repair *via* on-demand initiation and self-sustaining front-curing of aluminosilicate–epoxy composites, which are much more durable and sustainable than their ordinary Portland cement counterparts. Specifically, this work introduces a stable frontal curing strategy for aluminosilicate–epoxy composites that enables rapid underwater repair without external energy input in seawater, overcoming the chemical incompatibility between cationic epoxy curing and alkaline geopolymerization through a catalyzed stoichiometric formulation and waste-mediated water confinement to form robust 3D interpenetrating networks with rapid strength development and high durability under UV exposure and seawater immersion, demonstrating a KPI >87.4 fold higher than that of the state-of-the-art. Particularly, distinct from conventional UV light or electrically heated initiation methods, this work demonstrates an on-demand initiation method for the frontal curing *via* water-activated calcium oxide hydration, providing a compact, simple, and convenient route to trigger frontal curing for underwater repair applications.

1. Introduction

Rapid and durable underwater infrastructure repair techniques are highly valuable for the exploration of underwater resources as marine engineering continues to expand. As of 2024, the global underwater infrastructure repair market is valued at a total of $123.7 billion and is projected to grow at ~4–6% Compound Annual Growth Rate (CAGR).[1] Critical marine infrastructure, including subsea pipelines, offshore wind foundations, harbor structures, and undersea utility lines, faces a persistent risk of damage from synergistic effects of corrosion, impact, and extreme weather.[2] When failures occur, returning damaged components to a shore-based repair facility is often prohibitively time-consuming and labor-intensive, and in many cases, it is simply not feasible. Daily economic loss resulting from the downtime (primarily deferred production, repair expenses, and standby costs) for a damaged subsea pipeline can exceed $1 million per day.[2–4] While uncontrolled leaks pose threats to fisheries, coastal ecosystems, and water quality. The catastrophic economic and environmental consequences make rapid, durable underwater repairs extremely essential.

Under extreme seawater conditions, adhesive bonding is the most time-efficient repair approach, enabling *in situ* repair by

[a] Department of Materials Science and Engineering, Texas A&M University, College Station, Texas, USA. E-mail: S.Wang@tamu.edu
[b] Department of Industrial Systems and Engineering, Texas A&M University, College Station, Texas, USA
[c] Department of Mechanical Engineering, Texas A&M University, College Station, Texas, USA. E-mail: Jennyqiu@tamu.edu

directly filling the damaged region while maintaining operations.[5] Underwater adhesive systems typically rely primarily on two curing strategies: externally heated curing and environmentally triggered intrinsically self-curing. Externally heated curing, including infrared heating, joule heating, induction heating, dielectric heating, acoustic curing, and photo-curing, can be employed to supply thermal energy to accelerate crosslinking in cold seawater and accelerate the solidification process.[6–14] Unfortunately, they require substantial power, hardware, and operational support, making deployment in off-grid, deep-water, or emergency scenarios logistically challenging and costly, often impractical. In contrast, many efforts have been made to intrinsically cure by leveraging the surrounding environment to initiate and sustain curing without external power;[15–17] however, their curing rates are often limited by low seawater temperatures, leading to slow strength development and extended downtime before the repaired structure can safely resume full loading. Currently, the state-of-the-art method is to use ordinary Portland cement/epoxy hybrids for underwater repair *via* environmentally triggered, intrinsically self-curing, due to their low cost, bulk repair, and volume-filling capabilities.[15–17] Nevertheless, cement-filled epoxy hybrid materials exhibit weak bonding (<5 MPa) on a wet substrate, require a prolonged curing time (3 days to reach a minimum operational strength of 40 MPa), and, most importantly, have limited seawater resistance (loss $>40\%$ strength over one year[18]), posing significant constraints for offshore operations.

Advanced functional materials are sought to meet the enormous demand for underwater repair, which requires both rapid autonomous curing and seawater resistance. Geopolymer (GP), a crosslinked aluminosilicate cementitious material, is regarded as the most promising candidate for underwater repair functional materials, which exhibits outstanding seawater resistance, strong wet bonding capabilities, and high compressive strength to overcome the limitations of existing epoxy–cementitious adhesive hybrids.[19–21] Direct use of GP fails to meet the requirements for underwater repair due to its long curing time (28 days).[22,23] Some efforts have been made to incorporate saccharides and peroxides to accelerate the curing of geopolymers.[24] Such a formulation produces both gas (to generate pores/foam) and heat (to accelerate geopolymer curing), resulting in a foamed geopolymer. Unfortunately, this method yields low strength due to the highly foamed structure, and the compressive strength is only 0.21 MPa, too low for use in any repair. GP/epoxy systems were attempted; however, they cure at room temperature and still require approximately 7 days to reach a minimum operational strength of 40 MPa.[25,26]

Emerging frontal curing offers a new opportunity for the autonomous rapid curing of epoxy under seawater conditions by eliminating the need for external heating.[27–35] While epoxy resin can be cured under water, frontal curing of GP/epoxy hybrids is extremely challenging due to the inherent limitations of their curing chemistry. Epoxy frontal curing typically relies on cationic initiators, which generate highly reactive intermediates, superacids, to sustain the propagating cure front. In contrast, GP cures through alkali activation, requiring a strongly alkaline environment to break down aluminosilicate precursors and then geopolymerize into a durable cross-linked aluminosilicate network. Superacids and alkalis neutralize each other, disrupting both epoxy and geopolymer reactions and preventing a stable, self-sustaining cure front. Thus, cationic-initiator-based frontal curing of GP/epoxy hybrids faces a fundamental chemical challenge. Recently, free-radical frontal curing of GP/acrylate composites has been attempted in air; however, it requires an organic solvent (dimethyl sulfoxide) to dissolve the initiator and still yields low compressive strength (<19.3 MPa) and weak bonding due to the inherently low crosslink density of the acrylate polymer.[36] Solvent release and weak strength render GP/acrylate composites unsuitable for underwater repair. Consequently, front-curing GP/epoxy is highly desirable due to its potential for strong bonding capability for underwater repair.

Beyond the intrinsic limitations of curing chemistry in the frontal curing of GP/epoxy composites, frontal curing for underwater repairs requires effective, field-deployable initiation strategies. Thermal- and photo-initiation are the two principal initiation methods.[37] Thermal triggering typically involves the use of a soldering iron or an embedded resistive wire at a fixed voltage to heat a localized region, while photo-triggering typically uses UV light to activate photoacid generators for epoxide-ring-opening frontal polymerization.[38] Although the energy supply for the thermal initiation process is far lower than that of bulk heating, a bulk power apparatus is still required to initiate underwater frontal curing. For UV initiation, beyond the practical constraints of power delivery, the millimeter-scale penetration depth in water severely limits efficacy. Accordingly, an autonomous, self-powered initiation method is required to enable rapid curing in submerged environments.

In this paper, we developed a new class of functional materials, aluminosilicate–epoxy composites with well-designed stoichiometric formulations and catalytic curing agents, to enable multiple functions, including self-initiation and frontal curing, and exceptional seawater resistance for rapid underwater repair. Furthermore, an on-demand self-initiation method was developed to enable convenient, effective initiation of frontal curing in deep-water without requiring external energy, such as UV light or electrical heating, thereby greatly simplifying deepwater operation. The chemical and physical characterization of the exothermic materials and the frontal curing process was conducted to seek fundamental insights into the design of these novel functional materials. The resistance to marine conditions under accelerated UV ageing and seawater immersion was also examined.

2. Results and discussion

2.1. Material design for frontal-curing of GP/epoxy hybrids

The co-curing of GP and epoxy resin was investigated to create novel functional materials with stable frontal curing. The exothermic energy from the epoxy resin will be used to support GP curing simultaneously. Specific catalysts and amine curing agents were designed to ensure that the energy released from epoxy resins can continuously support both the GP and the epoxy itself for autonomous propagation. A water-activated

self-heating calcium oxide cartridge was intended for self-initiation on demand. Sorbitol polyglycidyl ether-based epoxy resin was mixed with *m*-xylylenediamine (*m*-XDA) and 1-methylimidazole for catalyzed ring-opening frontal polymerization to act as the fuel for rapid curing of GP/epoxy hybrids. Catalyzed frontal polymerization occurs by forming a reactive ring-opening nucleophile (amine–oxirane adduct) between amine and epoxy groups, which is compatible with the hydroxide group in the geopolymer–gel (G–gel) mixture.[39,40] The inclusion of catalysts facilitates nucleophilic activation of the epoxide, accelerating the formation of the ring-opening nucleophile.[41,42] Three types of Lewis base catalysts, including tertiary amine, pyridine, and imidazole, were evaluated for accelerating the epoxy–amine system. The most efficient catalyst, 4 wt%-1-methylimidazole, was identified from the reaction profile in Fig. S1a and b, which compensates for the typical slow curing rate of the amine–epoxy reaction and supports a stable front propagation (Fig. S1c). Mechanical properties of the frontal-cured optimized epoxy system are provided in Fig. S1d.

A natural aluminosilicate, metakaolin (MK), was used as the raw precursor for the inorganic GP phase, in the final composites. An alkaline solution containing sodium silicate and sodium hydroxide was selected as an activator to dissolve the MK and form the aluminosilicate monomer mixture (G–gel). It is noteworthy that the SiO_2/Na_2O molar ratio of the activator could influence the final properties of the GP. Therefore, we controlled the SiO_2/Na_2O molar ratio of the activator at 1.75 as reported in previous research for MK-based GPs.[43] To mitigate the negative effect of water evaporation on the rapid curing process and final properties of the composites, we introduced ground granulated blast-furnace slag (GGBFS) into the mixture, which could form the calcium–aluminate–silicate–hydrate (C–A–S–H) under an alkaline environment and then restrict the evaporation of free water during frontal curing.[44,45] The chemical composition of MK and GGBFS is listed in the Table S1, and the particle morphologies of MK and GGBFS are shown in Fig. S2. In addition, 1 wt% hydrophobic fumed silica (relative to the weight of the G–gel/epoxy mixture) was added to the final reactive mixture to improve the water resistance. A schematic illustration of the underwater frontal-curing concept is shown in Fig. 1. The self-heating cartridge, containing 1.4 grams of calcium oxide, can release heat upon activation by water. The temperature of the cartridge rose up to 102.4 °C at 210 s after contact with water, and gradually decreased to 55 °C within 700 s (Fig. 1b). Particularly, the surface temperature of the cartridge stayed above 80 °C for up to 215 s, which provides enough energy for triggering the rapid epoxy reaction. As revealed by the isothermal differential scanning calorimetry (DSC) characterization at 80 °C (Fig. 1c), the peak of the heat flow, which represents the highest curing rate, occurs at 50 s. The dynamic DSC analysis of the catalyzed epoxy also exhibits an S-shaped curing degree–temperature curve with a clear rate upturn starting around 75 °C (Fig. 1d). This onset confirms that the heating cartridge provides sufficient power to trigger the rapid epoxy reaction. After the successful initiation of the epoxy reaction, the intrinsic chemical energy in the epoxy group is released as fuel, heating the G–gel in the mixture and accelerating the polycondensation of the aluminosilicate monomers. Fig. 1e illustrates the accelerating effect of temperature on the initial and the final setting time of the G–gel applied in this work. The high temperature significantly accelerated the solidification of the G–gel, reducing the final setting time from 100 minutes at 20 °C to 7.6 minutes at 80 °C. This autonomous rapid-curing system contains a water-activated initiation cartridge and a self-sustaining fuel system. As shown in Fig. 1f, g and h, upon deliberate activation, the heat from the rapid calcium oxide hydration is transferred to a localized zone of the G–gel/epoxy mixture, triggering epoxy frontal polymerization (reaction mechanism illustrated with the structural formula is shown in Fig. S3). The heat released by epoxy ring-opening then sustains the reaction front and further elevates the temperature of aluminosilicate monomers, thereby accelerating their polycondensation. During frontal curing, co-curing of the G–gel and epoxy yields a GP/epoxy composite with excellent mechanical performance.

2.2. Thermochemical investigation of frontal curing

The unique frontal curing feature could be attributed to the delicate balance between self-heating initiation, the fast exothermic reaction of epoxy, heat loss to the environment, and dynamic heat transfer within the materials (Fig. 2a). Because the G–gel contains water that can cause substantial heat loss upon evaporation, we incorporate GGBFS to bind the water by forming C–A–S–H. The dynamic DSC test results in Fig. 2b revealed the effect of GGBFS on the endothermic evaporation of free water (Table S2 shows the composition of the specimens). The G–gel without GGBFS shows two endothermic peaks at 110 °C and 131 °C, corresponding to the evaporation of free water and combined water, respectively. After introducing GGBFS into the G–gel (S–G–gel), the two separated peaks merged into a broad peak and shifted to 135 °C. This indicates that free water was bound upon the addition of GGBFS. This GGBFS-induced confinement effect on free water could significantly reduce heat loss from water evaporation and benefit the frontal curing process. The DSC results of G–gel/epoxy and G–gel/epoxy with GGBFS added (S–G–gel/epoxy) confirmed our hypothesis. Incorporating GGBFS broadened and shifted the endothermic peak of water evaporation from 128.7 °C to 191.5 °C, reducing the endothermic dampening effect of water on the epoxy reaction and then enlarging the exothermic peak of epoxy polymerization. However, excess GGBFS could cause the G–gel to solidify immediately after mixing, leading to thickening of the mixture. After optimizing the addition of GGBFS, a 25 wt% GGBFS replacement of the MK was selected for further study (Fig. S4).

We further investigated how the mass ratio of G–gel to the epoxy system affected the frontal propagation at 25 wt% GGBFS addition. In the formulation of R-*Y*, *Y* represents the mass ratio of G–gel to epoxy. For better comparison of the frontal propagation, we utilized a constant temperature heating element (90 °C) for the initiation of the ambient frontal curing process. Fig. 2c shows that the intensity of the exothermic peak of epoxy polymerization decreased monotonically as the G–gel/epoxy

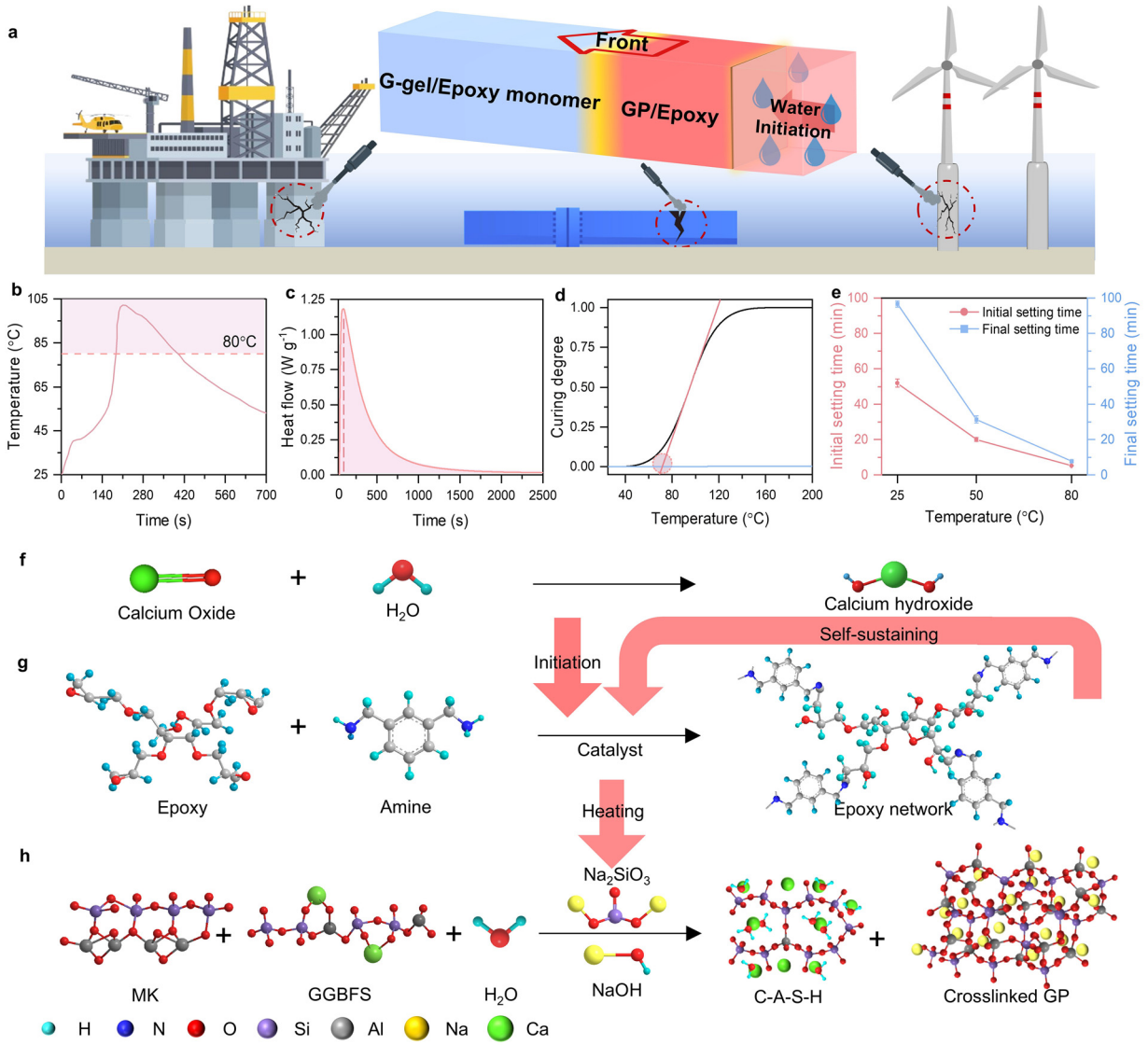

Fig. 1 (a) Schematic illustration of a new class of frontal curing of GP/epoxy composites, for underwater repair. (b) Temperature profile of the calcium oxide self-heating cartridge after activation with water. (c) Isothermal reaction profile of the catalyzed epoxy–amine reaction at 80 °C and (d) the dynamic curing degree profile of the catalyzed epoxy reaction at a temperature ramping rate of 20 K min^{-1}. (e) Effect of temperature on the initial and final setting times of GP materials. (f), (g) and (h) Reaction mechanism of the calcium oxide exothermic reaction, epoxy frontal polymerization, and GGBFS-participated geopolymerization. The red arrows indicate the direction of heat transfer.

mass ratio increased. At the same time, the exothermic peak shifted towards its original position (97.5 °C in DSC curves of the catalysed epoxy reaction, Fig. S1a), demonstrating a reduction in the endothermic inhibiting effect from water evaporation. Taking sample R-1.5/1 as a representative case, we utilized a thermographic visualization technique to analyze its frontal curing behavior. Fig. 2d shows time-resolved thermal images of the front propagation during the frontal curing process. From the time-resolved thermal images, the highest temperature was observed at the reaction front and stabilized at approximately 102 °C. Meanwhile, the position of the reaction front shifted over time at a stable rate, known as the frontal velocity, around 0.517 cm min^{-1}. Thermochemical simulation using the finite element method offers valuable insights into this frontal curing process (see Methods and Table S3). The snapshot of the simulated frontal curing process at room temperature for R-1.5/1 is shown in Fig. 2d. The simulated frontal temperature and frontal velocity were 106.5 °C and 0.54 cm min^{-1}, which were consistent with the experimental observation. Experimental frontal curing performance with various G–gel/epoxy mass ratios is illustrated in Fig. 2e. Consistent with the DSC results, an increase in the mass ratio results in a reduction in both the frontal temperature and velocity monotonically (Fig. 2e). However, excessive heat released from the polymerization of epoxy at a 0.5 : 1 mass ratio caused the frontal temperature to exceed 120 °C, which could facilitate water evaporation. When the mass ratio was at 1.5 and 2, in addition to a reduced frontal velocity, the frontal temperature also

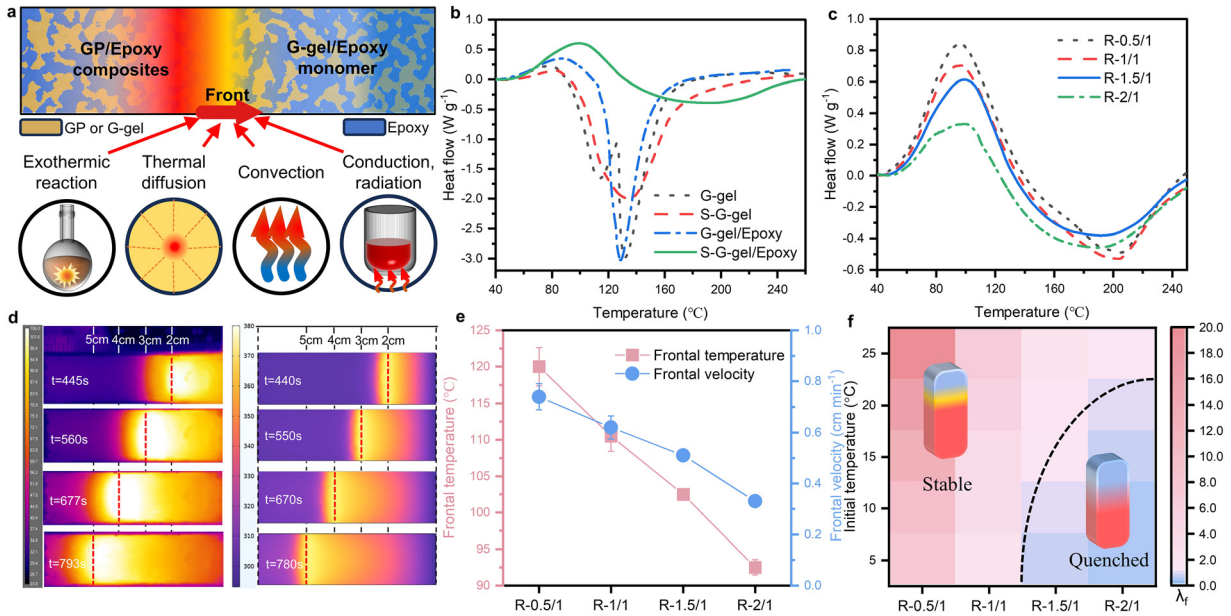

Fig. 2 Mapping compositions to stable frontal curing. (a) Schematic illustration of heat conservation for a control volume across the front-curing process. (b) GGBFS effect on restricting water evaporation. (c) Reaction profile against the temperature of the G–gel/epoxy mixtures with different G–gel-to-epoxy mass ratios. (d) Comparison of a series of time-resolved frontal-curing thermal images between experiment (left) and simulation (right). (e) Frontal temperature and frontal velocity with different mass ratios. (f) Numerical map of the initial mixture temperature with variation in the G–gel-to-epoxy mass ratio for the frontal curing process. Stable frontal curing processes are indicated in red, while those leading to quenched frontal curing processes are shown in blue (λ_f: thermal power density).

dropped to 102 °C and 92.5 °C, respectively. These lower temperatures are more suitable for GP curing. Photographs of all frontal-cured GP/epoxy specimens are presented in Fig. S5.

To further assess validity, we numerically mapped the stability window for frontal curing behavior across different G–gel/epoxy mass ratios, at various initial temperatures (Fig. 2f). The numerical analysis revealed that the spatial and temporal balance of thermal power density (λ_f) dictates the development of thermal stabilities during frontal propagation. The thermal power density is generated by the polymerization reaction (P_R, J m^{-3} s^{-1}), diffused by thermal transport (P_T, J m^{-3} s^{-1}) and lost *via* convection (P_c, J m^{-3} s^{-1})[46] (see Methods and Table S4). According to the experimental frontal performance at 25 °C, $\lambda_f = 1$ is considered the critical value for determining stability. Noticeably, as the G–gel-to-epoxy mass ratio increases from 0.5 to 2, the stability window gradually narrows. Isolating on an initial temperature of choice and moving rightward along the G–gel-to-epoxy mass ratio axis, an increased propensity for frontal quench is observed. These numerical results can mechanistically inform experimental design protocols, departing from inefficient approaches to the identification of stable frontal behavior.

2.3. Morphological and structural analysis of GP/epoxy composites frontal-cured in air

During the frontal curing process, the G–gel/epoxy mixture underwent epoxy polymerization and GP solidification. Optical microscopy (OM) and scanning electron microscopy (SEM) were used to characterize the polished surface and the cryo-fracture surface of frontal-cured GP/epoxy composites, respectively. Isolating on the optimized GGBFS content, 3D schematic visualization (cubic images) derived from 2D OM images in Fig. 3a shows how global morphology changes with the G–gel/epoxy mass ratio. With various mass ratios, phase macromorphologies changed from a globular morphology (0.5 : 1), to a discrete elongated morphology (1 : 1), then to a co-continuous morphology (1.5 : 1), and subsequently reverting to a discrete elongated morphology (2 : 1). In addition to the changes in phase morphology, macropore defects were observed on the surface of R-0.5/1, resulting from water evaporation during frontal curing with 120 °C frontal temperature. The corresponding phase microstructures are shown right below the phase morphology image. Cracks and pores were observed on the surface GP phase of R-0.5/1 and R-1/1, whereas R-1.5/1 and R-2/1 exhibited a compact GP-phase structure. The more compact GP phase could be attributed to lower frontal temperatures during the frontal curing process, suggesting that a frontal temperature below 110 °C is more suitable for GP curing.

Fourier-transform infrared spectroscopy (FTIR) and X-ray diffraction (XRD) were employed to reveal how the structural composition of the frontal-cured GP/epoxy composite developed. Before examining the influence of mass ratio, the effect of the GGBFS on the GP microstructure was confirmed (Fig. S6 and S7). The incorporated GGBFS could release calcium ions in an alkaline environment, generating C–A–S–H with a high surface area and nanopores in the GP phase (Fig. S7). This rapidly formed C–A–S–H can trap free water through strong hydrogen bonds that are formed by oxygen atoms in silicate and aluminate tetrahedra, as illustrated by the shift of the OH band in the

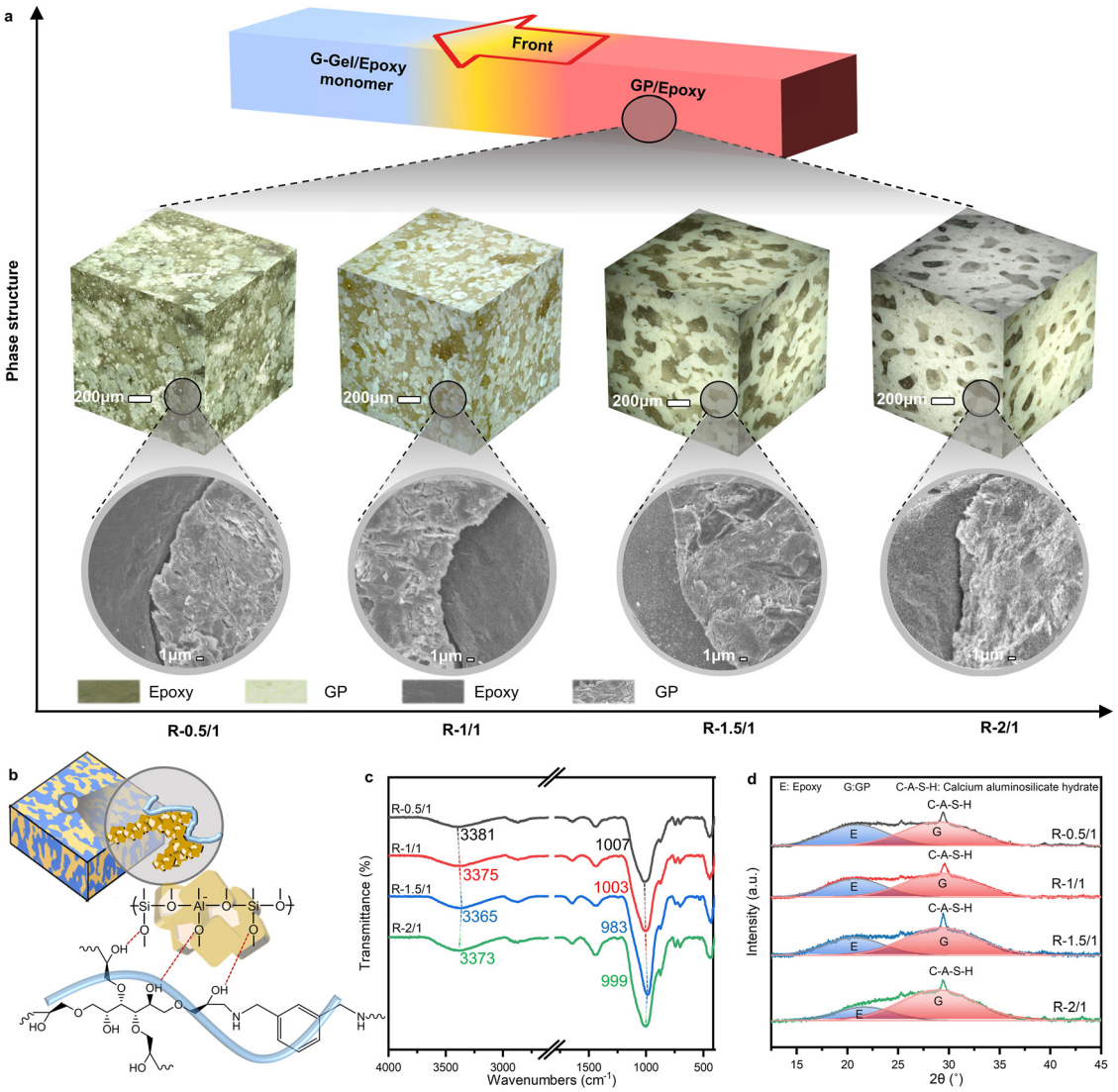

Fig. 3 Phase morphological and structural characterization of frontal-cured GP/epoxy composites. (a) Macro-(OM) and micro-phase evolution (SEM) of frontal-cured GP/epoxy composites with mass ratio. Upper row cubic image: 3D schematic visualization assembled from OM images of polished surfaces; lower row circular image: corresponding SEM microstructures. (b) Illustration of the hydrogen bond formation between epoxy resin and aluminosilicate. (c) FTIR spectra of OH and Si–O–T stretching peaks for R-samples (the color-coded dashed line represents the shift trends of OH and Si–O–T peaks). (d) XRD spectra of frontal-cured samples (devolution of the XRD spectra into epoxy (blue) and GP (red) amorphous peaks).

FTIR curves (Fig. S6). In addition to hydrogen bonds within the GP phase, interfacial hydrogen bonds can form between the GP and epoxy phases, as schematically illustrated in Fig. 3b (the red line indicates the hydrogen bonds). The oxygen atoms in the silicate and aluminate tetrahedra in the GP phase can form hydrogen bonds with the epoxy network's hydroxyl (OH) groups, resulting in a compact microstructure for the GP–epoxy network.

The influence of the G–gel/epoxy mass ratio is illustrated in Fig. 3c and d. The typical broad band of stretching vibrations of OH groups in R-1.5/1 shifted to the lowest wavenumber (3365 cm^{-1}) compared to the samples with other mass ratios, suggesting the build-up of more hydrogen bonds between the GP phase and epoxy (Fig. 3c). Another major peak at 1034.9 cm^{-1} of the asymmetric stretching vibration of Si–O–T bands (T is tetrahedral silicon or aluminum) in raw aluminosilicate precursors (Fig. S6) shifted to a lower wavenumber range between 983 and 1011.5 cm^{-1} due to the partial substitution of SiO_4 tetrahedra by AlO_4 tetrahedra after geopolymerization. The lowest wavenumber (983 cm^{-1}) of the Si–O–T band in R-1.5/1 represented the highest degree of GP curing. Stronger hydrogen bonding and higher GP phase cure degree both contribute to a more compact co-continuous, interlocking microstructure of R-1.5/1 observed by OM and SEM, which is driven by the optimum frontal temperature and the increased interfacial contact. After the frontal curing process, epoxy and GP in the composites presented a broad diffraction hump in 2θ = 13.5–32° and 2θ = 20–37.5° ranges (Fig. 3d), respectively, illustrating the amorphous phase of the disordered polymer network and aluminosilicate structure. The intense peak at 2θ = 29.4° represented the dominant feature of C–A–S–H.[47] The typical broad

diffraction hump range observed at 2θ = 18–32° for amorphous Si–O–T in metakaolin (Fig. S7) shifted to a higher range of 2θ = 20–37.5°, demonstrating the dissolution of the original amorphous phase in metakaolin and the rearrangement to a new compact amorphous GP phase in the composites.[48] This typical characteristic hump for amorphous aluminosilicate phase in the XRD patterns of R-1.5/1 shifted to the highest scattering angle of 2θ = 20–39°, centered at 2θ = 29.5°, reflecting the highest degree of geopolymerization of the GP phase, which was also consistent with the morphology development shown in the SEM results and the Si–O–T band changes characterized in FTIR.

2.4. Mechanical properties and durability of GP/epoxy composites frontal-cured in air

For ambient frontal-cured GP/epoxy composite samples with various mass ratios, both the compressive and flexural strengths exhibit changing trends that initially increase and then decrease. This trend shows a turning point occurred at a 1.5 : 1 G–gel-to-epoxy mass ratio (Fig. 4a). At this composition, the frontal temperature during the frontal curing process was controlled at 102 °C, effectively suppressing the water evaporation while simultaneously accelerating the geopolymerization. Moreover, a co-continuous, interlocking network with a compact microstructure was formed at this mass ratio. Consequently, the specimen R-1.5/1 exhibited the best mechanical properties, characterized by a compressive strength of 61.01 MPa and a flexural strength of 21.80 MPa. Frontal-cured GP/epoxy composites exhibited better mechanical properties than conventionally (oven and ambient) cured pure GPs (GP-O and GP-R) (Fig. 4b). Specifically, GP-O shows higher compressive stress (49.01 MPa) and flexural stress (5.44 MPa) than the compressive stress (35.11 MPa) and flexural stress (3.39 MPa) of GP-R, verifying the heating promotion effect on GP curing. Meanwhile, frontal-cured GP/epoxy composites show mechanical properties comparable to conventionally (oven) cured GP/epoxy composites, showing only a 6% reduction in compressive strength and a 5.2% reduction in flexural strength, indicating that the frontal curing strategy could provide the energy necessary for the crosslinking of the epoxy monomer and the curing of the GP.

In particular, the mechanical behavior of the GP/epoxy-frontal curing sample (R-1.5/1) and GP-O reference samples was examined by plotting the representative complete stress–strain response (Fig. 5c and d). As already demonstrated, the composite sample shows a higher strength than the neat GP. More notably, toughening behavior was observed in their stress–strain curves. The peak stresses of both the compression and bending curves occur at much higher strains than those in GP-O. In addition, the compressive stress–strain curve related to the GP/epoxy-frontal cured sample continuously stepped at a high stress value after the maximum stress occurred, and the shape of the flexural stress–strain curve transformed from a brittle failure mode (linear rise-rapid loss) to a ductile failure mode (non-linear rise-yield loss). The representative stress–strain curves of other GP/epoxy specimens are presented in Fig. S8 and S9.

To further elucidate the toughening mechanism, we further examined GP/epoxy-frontal cured (R-1.5/1) and GP-O samples in the single-edge notched bending test to compare the crack propagation *via* digital image correlation (DIC) technology (Fig. 4e). Unlike the GP's linear crack propagation path, the crack propagated along a serpentine path in the GP/epoxy-frontal cured sample. In the GP/epoxy-frontal cured composites with a co-continuous phase morphology, when the crack reaches a weak interface, the stress on the crack can easily break the interface, causing crack deflection. The zigzag crack path inherently elongated the crack, thereby absorbing more energy. In addition to

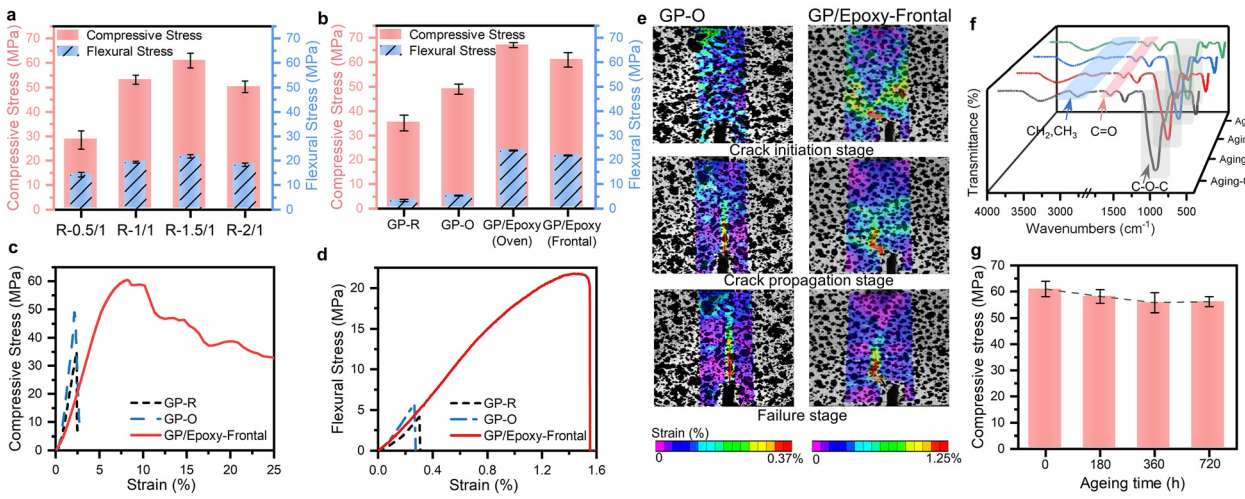

Fig. 4 Mechanical performance and durability of the composites. (a) Compressive strength and flexural strength of frontal-cured-GP/epoxy with various G–gel-to-epoxy mass ratios. (b) Comparison of the compressive strength and flexural strength of frontal-cured-GP/epoxy with those of reference speciemens. (c) Representative compressive stress–strain curves and (d) flexural stress–strain curves of R-1.5/1 compared with those of GP reference specimens. (e) Diagrams of the transverse strain of GP-O and GP/epoxy-frontal-cured composites at different crack stages. (f) FTIR spectra of R-1.5/1 under different UV exposure durations (blue-coded region CH_2 and CH_3 peaks, red-coded region C═O peaks, and gray-coded region C–O–C peaks). (g) Compressive strength evolution of R-1.5/1 with the accelerated UV aging time.

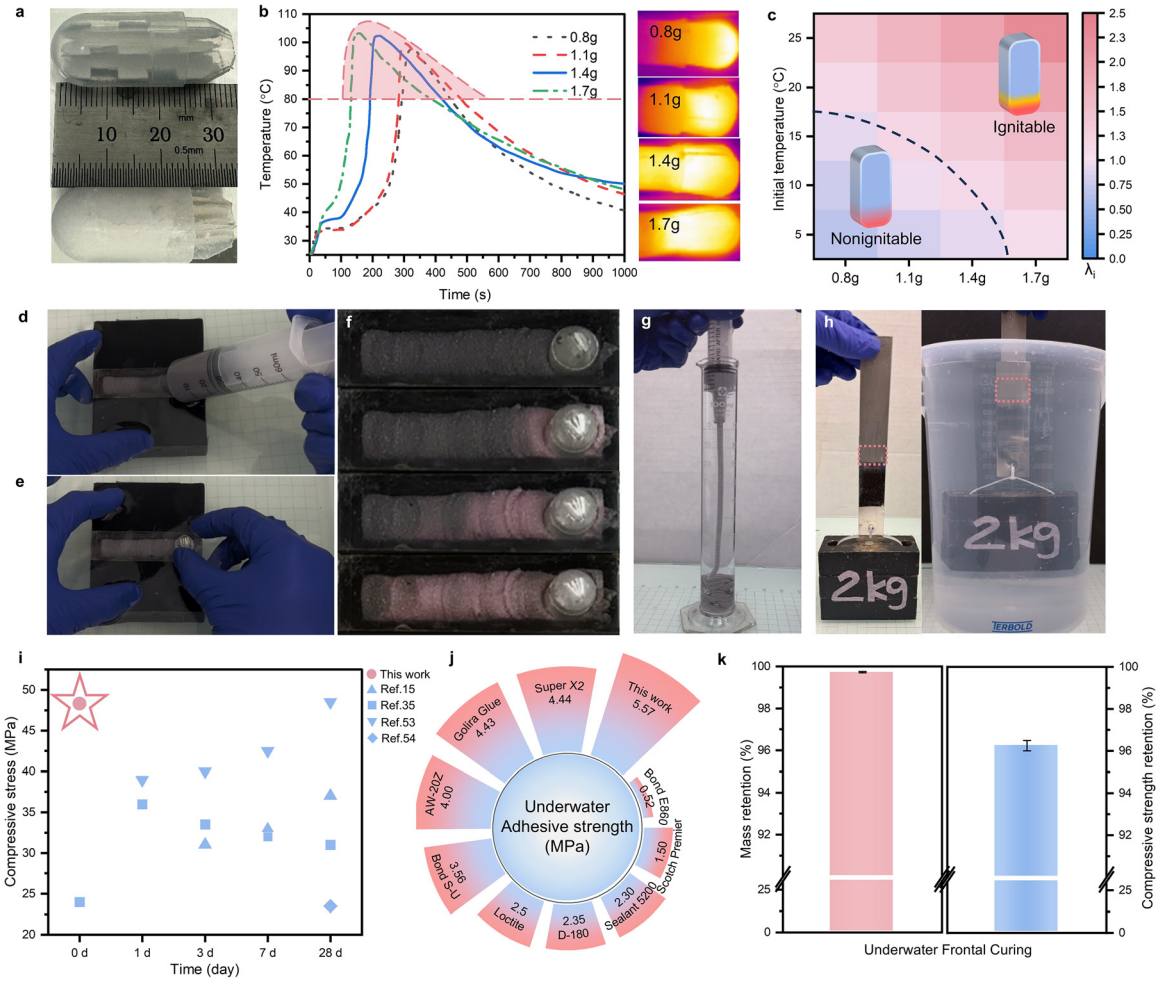

Fig. 5 Evaluation of the underwater frontal curing initiated by the calcium oxide cartridge. (a) Photograph of the calcium oxide self-heating cartridge with an origami-based water-absorbing wick. (b) Heating profiles of calcium cartridges accompanied by the corresponding IR photos at the highest temperature. (c) Initiability map of cartridges at various initial temperatures for the frontal curing process of R-1.5/1 composition. (d)–(f) Photographs of the underwater frontal curing process initiated by the 1.4 g-calcium oxide cartridge of GP/epoxy composites with a 1.5 : 1 G–gel-to-epoxy mass ratio. (g) Underwater macroscopic test of the non-dispersibility of the G–gel/epoxy reactive mixture. (h) Photographs of the single lap joint with underwater frontal-cured GP/epoxy lifting a weight of 2 kg (red dashed box represents the bonding area). (i) Comparison of the compressive stress of underwater frontal-cured GP/epoxy with other reported underwater-cured epoxy cementitious composites. (j) Adhesive performance of underwater frontal-cured GP/epoxy compared with typical commercial underwater repair materials. (k) Seawater resistance performance of GP/epoxy-frontal-cured specimens (compressive strength retention and mass retention).

the crack deflection, another toughness mechanism was the ductile crazing induced by the epoxy phase. Crazing developed in front of the crack, leading to micro-void formation. These voids propagated in a plane normal to the stress stabilized by the fibrils spanning the crack temporarily. As the crack propagated, the epoxy fibrils were drawn, crept, and eventually broke down, absorbing extensive fracture energy (Fig. S10b). These mechanisms occurring within the GP/epoxy-frontal curing composites enhanced the material's toughness and helped prevent catastrophic fracture.

Durability is a critical property for epoxy-based cementitious materials applied in underwater repair, as they are often exposed to moisture, large temperature differences, sustained ultraviolet (UV) radiation, and other harsh environments. Therefore, it is essential to test the durability of the GP/epoxy-frontal curing system under these aging conditions. An accelerated UV aging test was conducted under controlled moisture and cycling temperature conditions (see Methods for details) to evaluate its durability. The chemical composition evolution of the GP/epoxy-frontal curing (R-1.5/1) system under different accelerated-UV aging durations was investigated by FTIR (Fig. 4f). It is confirmed that the consequence of UV exposure under vapor condensation on epoxy could cause photo-oxidative degradation, which changed the chemical composition of epoxy by depleting the aliphatic CH_2 and CH_3 groups (2911 cm^{-1} and 2868 cm^{-1}), cleavage of the C–O–C bond (1070 cm^{-1}) and forming carbonyl ((C═O) groups[49–52] (Fig. S11a). However, after the initial 180 hour aging test, only slight changes in the chemical groups were observed in the GP/epoxy-frontal curing, and further accelerated UV aging (360 h and 720 h) did not

cause any significant additional changes in the intensity of the characteristic functional groups. The mechanical properties of the aged GP/epoxy-front curing showed only a slight reduction during the first 180 hours of aging, with strength decreasing from 61.01 MPa to 58.17 MPa. After that, the strength stabilized around 56.00 MPa, retaining approximately 92% of the original value even after 720 hours of accelerated aging (Fig. 4g). This excellent durability performance originated from the GP phase in the co-continuous structure, preventing further aging of the epoxy, due to its strong Si–O–Al bonds in the compact crosslinked GP structure (Fig. S11b).

2.5. Underwater frontal curing of GP/epoxy composites

The ability for autonomous frontal curing provides a potential way for rapid underwater repair. Inspired by self-heating food packaging and considering the extreme power-limited conditions underwater, we utilized a water-activated self-heating calcium oxide cartridge (Fig. 5a) to initiate the frontal curing process underwater. Specifically, the calcium oxide was filled in a separate cartridge container as an external initiation source, rather than being incorporated into the GP/epoxy reactive mixture. The amount of calcium oxide in the self-heating cartridge determines the initiation temperature and duration, as illustrated by the temperature profiles recorded after water activation (Fig. 5b). Based on the DSC analysis of the epoxy reaction kinetics shown in Fig. 1c and d, a temperature of 80 °C was set as the starting point of the rapid catalytic reaction of the epoxy system. Therefore, intervals in which the temperature exceeds 80 °C are defined as effective initiation intervals (marked in red in Fig. 5b). The average temperature and duration of this interval are taken as the effective initiation temperature and effective initiation time, respectively. Both the initiation temperature and duration increase with the amount of calcium oxide, while the growth accelerates at 1.1 grams and slows down at 1.4 grams. The IR images captured at each cartridge's peak temperature are presented in Fig. 5b, visualizing the extent of the exothermic response. To further assess the triggering validity, we numerically map the ignitability window of the self-heating cartridge across different calcium oxide amounts at various initial temperatures. The thermal power density (λ_i) generated by the polymerization reaction (P_R, J m^{-3} s^{-1}) at the effective initiation temperature, diffused by thermal transport during the effective initiation time (P_T, J m^{-3} s^{-1}) and lost *via* convection (P_C, J m^{-3} s^{-1}) reveals the development of the initiability of the cartridges (see Methods and Table S5). When the heat generated by the epoxy reaction at the initiation temperature exceeds the diffused and convected-losses ($\lambda_i > 1$), the frontal curing process is initiated. When heat diffuses away and convects to the environment faster than the heat generated by polymerization at the initiation temperature ($\lambda_i < 1$), the self-heating cartridge won't trigger the frontal curing process. Therefore, $\lambda_{i=1}$ is the critical value for illustrating the initiability.

According to the ignitability analysis, a 1.4 gram cartridge was selected to demonstrate the underwater frontal curing process of GP/epoxy composite with a 1.5 : 1 G–gel-to-epoxy mass ratio (thermochromic power was incorporated to visualize the curing front, color changing from black below 35 °C to pink above 35 °C). Snapshots of the extrusion, initiation, and frontal curing process from Video S1 are shown in Fig. 5d–f. The reactive G–gel/epoxy mixture was injected into the channel of the mold through a syringe (Fig. 5d), followed by the insertion of a calcium oxide self-heating cartridge (Fig. 5e). Upon manual activation of the self-heating cartridge, water permeated the cartridge through the distributing wick and reacted with the calcium oxide to release heat. A pink reaction front can be observed 8 minutes after the calcium oxide cartridge comes into contact with water. Then, the pink reaction front self-propagated with a 0.3 cm min^{-1} frontal velocity and 88 °C frontal temperature (Fig. 5f). Photographs of the underwater frontal-cured specimen are shown in Fig. S12. This demonstration successfully validated the underwater frontal curing process in confined channel- and joint-type geometries representative of crack repair.

Effective underwater repair requires materials with good anti-dispersion properties, high structural stability under load (compressive strength and adhesive strength), and robust seawater resistance. Fig. 5g illustrates the favorable underwater workability of the non-dispersible G–gel/epoxy reactive mixture, demonstrating that it can be directly deposited on repair substrates. Macroscopic adhesive tests confirmed that there was no displacement or separation that occurred at the single lap joint after hanging a weight of 2 kg underwater (Fig. 5h). From a comparison of the compressive strength of underwater-cured epoxy cementitious materials,[15,35,53,54] it was clearly shown that the underwater frontal-cured GP/epoxy materials exhibit the most rapid strength development and achieve the highest compressive strength (Fig. 5i). Using the ratio of compressive strength (MPa) to the curing time (hours) as the key property indicator (KPI), this work demonstrated more than 30-fold improvement against the alternatives in the underwater curing. The adhesion strengths of underwater frontal-cured GP/epoxy were compared with those of typical commercial underwater glues on steel substrates in Fig. 5j.[55] The comprehensive comparison clearly showed that the adhesive strength in this work outperformed that of commercial underwater adhesives on steel. This enhancement is attributed to the formation of Al–O–Fe chemical bonds at the interface between the GP and the steel surface.[56] Compressive strength and adhesive strength of underwater frontal-cured GP/epoxy specimens show 20.5% and 22.6% reduction compared to those of ambient frontal-cured specimens due to the decreased frontal temperature and rapid cooling in the post-frontal curing process (Fig. S13). However, the immediate compressive strength (48.3 MPa) and adhesive strength (5.57 MPa) of GP/epoxy after the underwater frontal curing process satisfy the standard handling strength ($\sim$40 MPa) and structural repair requirements.[15] A seawater corrosion test was also conducted on frontal-cured GP/epoxy specimens (R-1.5/1). As illustrated in Fig. 5k, underwater frontal-cured specimens maintain 96.25% of the initial compressive strength and 99.74% of the initial mass after 7 days of immersion in seawater (surface morphological changes are shown in Fig. S14). The frontal-cured GP/epoxy composites exhibited excellent seawater resistance due to the crosslinked aluminosilicate

network in the GP phase and their compact co-continuous phase structure.

3. Conclusions

Frontal curing of aluminosilicate/epoxy composites for underwater repair has been developed. The formulation of the aluminosilicate/epoxy composites was optimized to achieve a co-continuous, interlocking network, resulting in outstanding mechanical performance, with a front temperature of 88 °C and a frontal velocity of 0.3 cm min^{-1}. The key property indicator (KPI), defined by the ratio of minimal operational compressive strength to the required curing time, outperforms state-of-the-art performance by 87.4-fold. The resulting composite demonstrated outstanding seawater resistance, retaining 92% of its original strength after 720 hours of exposure to UV radiation and thermal cycling, and exhibiting 99.74% mass retention and 96.25% strength retention after 7 days of seawater exposure. This research presents a novel aluminosilicate/epoxy composite as a functional material for rapid and durable deepwater repair, demonstrating marine environmental stability that meets or exceeds relevant industry standards.

4. Experimental and methods

4.1. Materials

Metakaolin (MK) was purchased from Engelhard; GGBFS was provided by Heidelberg Materials; sodium silicate solution (7.5–8.5% Na_2O; 25.5–28.5% SiO_2, Supelco), sodium silicate (for analytical purposes), sodium hydroxide (reagent grade, ≥98%), *m*-xylylenediamine (*m*-XDA) (99%), 3-(trimethoxysilyl)-propylamine (APTMS) (99%), 1-methylimidazole (IM) (99%) 2,4,6-tris(dimethylaminomethyl)phenol (DMP30) (95%), and 4-(dimethylamino)pyridine (DMAP) (99%) were purchased from Sigma; hydrophobic fumed silica was supplied by Applied Materials Solution. Epoxy (ERISY GE-60) was purchased from Azelis (an aliphatic tetrafunctional epoxy resin with an epoxy equivalent weight of about 178 g $eq.^{-1}$ and a viscosity of 8000–18 000 mPa·s at 25 °C). The thermochromic pigment was purchased from Atlanta Chemical Engineering.

4.2. Preparation of the G–gel/epoxy mixture

The optimized sample R-1.5/1 is taken as an example. To prepare the G–gel/epoxy mixture, an alkaline activator was first prepared 1 day before use by mixing sodium silicate solution (100 g) with sodium silicate (8 g) and sodium hydroxide (9 g) using a mechanical mixer (Benchmark IPS2050-20) at 300 rpm. Metakaolin (67.5 g) and GGBFS (22.5 g) were added to the prepared alkaline activator, followed by 5 minute mixing at 300 rpm to form the G–gel. At the same time, epoxy (116 g) and *m*-XDA (22 g) (1 : 1 stoichiometric ratio) and 4 wt% imidazole (4.84 g) relative to epoxy were also pre-mixed for 1 min by mechanical stirring at 500 rpm. After that, the epoxy mixture and G–gel were mixed for 3 min at 500 rpm, followed by adding 1 wt% fumed silica relative to the total weight of the mixture and mixing for another 3 min at 500 rpm in an ice bath. Finally, the mixture was degassed on a vibratory platform for 10 min to remove trapped air and ensure homogeneity and then stored immediately in ice for future use.

For the G–gel/epoxy mixture used to demonstrate underwater frontal curing, a thermochromic powder (1 wt% relative to the epoxy) was incorporated by mechanical mixing at 500 rpm for 3 min prior to degassing to visualize the movement of the reaction front.

4.3. Frontal curing of GP/epoxy composite implementation

For the ambient frontal curing process, after the G–gel/epoxy mixture was prepared, the material was cast using a syringe into a silicone mold (15 m × 20 mm × 70 mm). Then, a constant temperature heating element (90 °C) was inserted into one side of the mixture to initiate the frontal curing process. The frontal temperature evolution of the ambient frontal curing process was recorded on an infrared thermal camera (FLIR A325sc). After 3 minutes of initiation, the reaction front can be noticed by the self-propagation of the bright glowing front *via* thermographic visualization. For the underwater frontal curing process, the calcium oxide self-heating cartridge was used for initiation. The temperature evolution was recorded using embedded thermal sensors.

GP-R was prepared by casting the G–gel in a mold and then sealing it for curing at room temperature for 28 days. GP-O samples were cured in an oven, following the room temperature – one day and 80 °C – 28 days curing steps. GP/epoxy-oven was cured in the oven at 80 °C for 24 hours. GP/epoxy-frontal was cured by the ambient frontal curing process.

4.4. Finite element simulation

The numerical modeling was conducted using COMSOL Multiphysics 6.0, a finite element analysis platform, to simulate the self-sustaining frontal curing process. Geopolymerization is relatively weakly exothermic compared with the rapid heat release of epoxy polymerization over short timescales. In addition, at the optimized formulation, GGBFS introduces a water-evaporation confinement effect. Under these conditions, frontal initiation and propagation of the G–gel/epoxy mixture can be described by a model that couples the heat-exchange eqn (1) with the epoxy cure-kinetics eqn (2) as follows:

$$k\nabla^2 T + (1-\phi)\rho H_r \frac{\partial \alpha}{\partial t} = \rho C_p \frac{\partial T}{\partial t} \quad (1)$$

$$\frac{\partial \alpha}{\partial t}(\alpha, T) = A(1-\alpha)^n \alpha^m \exp\left(\frac{-E_a}{RT}\right) \quad (2)$$

where k is the thermal conductivity (W m^{-1} K^{-1}), ∇T is the temperature gradient (K m^{-1}), C_p is the heat capacity (J kg^{-1} K^{-1}), ρ is the density (kg m^{-3}), H_r is the total enthalpy of the epoxy reaction (J g^{-1}), T is the temperature (Kelvin), and ϕ denotes the volume fraction of the G–gel. In eqn (2), A is the pre-exponential factor (s^{-1}), E_a is the activation energy (J mol^{-1}), and R is the universal gas constant (=8.314 J mol^{-1} K^{-1}), α is the related degree of cure of epoxy at time t. n and m are the two exponents entering the Prout–Tompkins model. The cure

kinetics parameters A, E_a, n, and m are found by the nonlinear fitting of curing data extracted from dynamic DSC tests (Table S3).

Assuming that the G–gel/epoxy mixture is a homogeneous system, the C_p, k, and ρ can be estimated using the rule of mixtures, as follows:

$$C_p = C_{p,E}(1-\phi) + C_{p,G}\phi,\ k = k_E(1-\phi) + k_G\phi,\ \rho = \rho_E(1-\phi) + \rho_G\phi \quad (3)$$

where subscripts E and G represent epoxy and the G–gel.

The values and sources of the constants used in the equation in the COMSOL software are listed in Table S3. The thermal conductivity and heat capacity of the G–gel were measured by Hot Disc thermal conductivity analysis. The densities of the epoxy and G–gel were measured from a standard sample by taking the mass divided by the volume of the sample.

Assuming that all the heat released during polymerization is used for front propagation, we define the maximum temperature (T_{max}) associated with the front as:

$$T_{max} = T_0 + (1-\phi)(1-\alpha_0)\frac{H_r}{C_p} \quad (4)$$

The ratio of power densities for stability (λ_f) was computed as follows:

$$\lambda_f = \frac{P_R}{P_T + P_C} = \frac{\rho(1-\phi)H_r A e^{-E_a/(RT)}}{\kappa\frac{T}{L_f^2} + h\frac{P}{S}(T_{max} - T_0)} \quad (5)$$

where T_0 (K) is the initial temperature, T (K) is the average of the initial and maximum temperatures, h (W m^{-2} K^{-1}) is the heat transfer coefficient, L_f (m) is the width of the thermal front, and P (m) and S (m^2) denote the perimeter and the area of the channel's cross-section, respectively.

The ratio of power densities for initiability (λ_i) was computed as follows:

$$\lambda_i = \frac{P_R}{P_T + P_C} = \frac{\rho(1-\phi)H_r A e^{-E_a/(RT')}}{\kappa\frac{T'}{L_d^2} + h\frac{P}{S}(T_i - T_0)} \quad (6)$$

$$L_d = 2\sqrt{\kappa t_i/\rho C_p} \quad (7)$$

where T_i (K) is the effective initiation temperature, T' (K) is the average of the initial and effective initiation temperature, t_i (s) is the effective initiation time, and L_d (m) is the thermal diffusion length.[57]

4.5. Characterization techniques

4.5.1. Heat of reaction. Differential scanning calorimetry (DSC) measurements were employed on a DSC (Q20, TA Instruments) equipped with a CFL-50 cooling system. The measurements were performed in the temperature range 25–260 °C, at a ramping rate of 20 K min^{-1} with a nitrogen flow rate of 50 mL min^{-1}.

4.5.2. Setting time of the GP. Vicat needle measurements were performed to evaluate the temperature effect on the initial setting time and final setting time of the GP according to ASTM C191.

4.6. Characteristics of the frontal behavior

The front temperature and velocity of ambient-frontal curing were calculated from infrared recordings that comprise a time-resolved thermal map at a frame rate of 27 Hz. The front temperature and velocity of underwater-frontal curing were calculated from the time-resolved temperature profile recorded using thermal sensors.

4.7. Microstructure characterization

An Olympus BX51 fluorescence microscope and scanning electron microscope (JEOL JSM-7500F) at an accelerating voltage of 20 kV was used to perform phase morphology and microstructure analysis. The X-ray diffraction (XRD) spectra of the samples were recorded on a Bruker D8 Discover diffractometer at a voltage of 40 kV and a current of 40 mA with CuKα (λ: 1.5418 Å) radiation at room temperature from 10° to 70°. The chemical composition and group changes of the samples were analyzed by scanning in the wavelength range of 400–4000 cm^{-1} *via* Fourier-transform infrared spectroscopy (FTIR) using a Bruker Alpha-Platinum spectrometer.

4.8. Mechanical testing

The compression test, flexural test, and the lap shear strength test were carried out using an MTS test machine with 30 KN load cells. Compressive strength tests of GP-R, GP-O, GP/epoxy-oven, and GP/epoxy-frontal curing samples with dimensions of 15 mm × 15 mm × 20 mm were carried out according to ASTM C109. The loading rate was set to 2 mm min^{-1} with a preload force of 0.5 N. For flexural testing, samples with dimensions of 10 mm × 10 mm × 45 mm were evaluated according to ASTM C293 M-10. The loading rate was 1 mm min^{-1}. L-304 stainless steel was used as the substrate for the lap shear strength test (ASTM D1002). Before the test, the surface of the adhesive region was abraded with 120 grit sandpaper. The specimens with a bonding thickness of 2 mm were prepared for the lap shear strength test. The loading rate was chosen to be 1 mm min^{-1}. Each group had at least three specimens.

For underwater frontal-cured lap shear specimen preparation, the reactive mixture was directly deposited on the steel plate underwater to make the single lap joint. Then, a heating element with constant temperature (90 °C) was used to heat the top side of the joint for 3 min to simulate the initiation of the calcium oxide heating cartridge.

4.9. Digital image correlation (DIC) test

Digital Image Correlation technology was adopted for monitoring and quantifying the crack deformation during the single notched three-point bending test according to ASTM D5045-99. For DIC analysis, a random speckle pattern was created by spraying black matte paint on the white-painted surface of the GP and frontal-cured GP/epoxy specimens (35 mm × 35 mm × 125 mm). Fig. S9 shows the equipment and specimens used for the DIC test. The loading rate for the three-point bending test

was 0.2 mm min^{-1} to control the shooting time of a digital camera (Canon EOS 77D).

4.10. Accelerated UV aging test

The accelerated UV aging test of frontal-cured GP/epoxy specimens, combining the actions of UV radiation, vapor condensation, and thermal cycling, was performed in a UV light accelerated aging test chamber (SB-UVA 340 nm). A UV aging period of 720 h was employed, alternating the cycles of UVA radiation (8 h) at 60 °C of 0.9 W m^{-2} and water condensation (4 h) at 50 °C. Tests were conducted according to ASTM G 154-00a. The compressive properties and FTIR spectra of the samples were recorded at 180 h, 360 h, and 720 h.

4.11. Seawater resistance

The mass loss and compressive strength loss of frontal-cured cylindrical specimens (∅ 17 mm × 20 mm) after 7 day immersion in artificial seawater were measured to assess the resistance against seawater attack. Artificial seawater was fabricated according to the standard ASTM D1141.

Conflicts of interest

The authors have filed a patent for this work (Aolin Hou, Jingjing Qiu, and Shiren Wang, Patent Application number: 63/968,999). There are no other conflicts to declare.

Data availability

The data supporting the findings of this study are available within the article and its supplementary information (SI). Supplementary information is available. See DOI: https://doi.org/10.1039/d5mh02462e.

Additional data are available from the corresponding author upon request.

Acknowledgements

The authors are grateful for the funding support from the Department of the Interior and the Offshore Energy and Safety Institute (Award #E21AC00000-00).

References

1 Published by Grand View Research, 2025, Report ID: GVR-4-68040-529-1.
2 F. Y. Jiang and E. J. Zhao, *Ocean Eng.*, 2025, **318**, 120119.
3 DAPL shutdown would 'shock' economy: Energy Transfer, (accessed).
4 C. Prescott and D. Brower, US20050283276A1, 2005.
5 T. Zheng, L. Lin, X. Zhang, X. Bian, K. Shao, G. Sun, X. Wang, L. Zhang and J. Shen, *Polym. Compos.*, 2026, **47**, 3775–3788.
6 D. Odiyi, T. Sharif, R. Choudhry, S. Mallik and S. Shah, *Composites, Part B*, 2023, **267**, 111034.
7 M. G. Collinson, T. J. Swait, M. P. Bower, B. Nuhiji and S. A. Hayes, *Composites, Part A*, 2023, **172**, 107615.
8 D. J. Kim and C. H. Ahn, *IEEE Access*, 2025, **13**, 79237–79246.
9 C. B. Sweeney, A. G. Moran, J. T. Gruener, A. M. Strasser, M. J. Pospisil, M. A. Saed and M. J. Green, *ACS Appl. Mater. Interfaces*, 2018, **10**, 27252–27259.
10 M. M. Karimi, H. Jahanbakhsh and F. M. Nejad, *Constr. Build. Mater.*, 2021, **273**, 121762.
11 C. Yue, Y. Zhang, W. Lu, Y. Zhang, P. Wang, Y. Li and H. Zhou, *Composites, Part A*, 2022, **163**, 107181.
12 M. Ouyang, W. Tian, Y. Liu and W. Wang, *Constr. Build. Mater.*, 2022, **330**, 127279.
13 S. Genty, P. Tingaut and M. Aufray, *Thermochim. Acta*, 2018, **666**, 27–35.
14 P. Dhakal, R. Liu, J. G. Kim, A. Hou, X. Wu and S. Wang, *J. Neuromorph. Intell.*, 2024, **1**, 21–30.
15 X. S. Han, F. Xu, J. Y. Ge, W. X. Qian, Y. He, X. Y. Meng and P. F. Zhu, *Constr. Build. Mater.*, 2025, **462**, 139966.
16 S. Kim, J. H. Yi, H. Hong, S. I. Choi, D. Kim and M. O. Kim, *Polymers*, 2023, **15**, 4290.
17 J. J. Assaad, N. Gerges, K. H. Khayat, N. Lattouf and J. Mansour, *ACI Mater. J.*, 2019, **116**, 169–178.
18 P. Ghassemi and V. Toufigh, *Constr. Build. Mater.*, 2020, **234**, 117887.
19 G. K. Erguler and A. D. Taleghani, *Environ. Earth Sci.*, 2025, **84**, 345.
20 H. Li, Z. H. Zhang, Y. L. Deng, F. Xu, J. Hu, D. J. Zhu, Q. J. Yu and C. J. Shi, *Cem. Concr. Comp.*, 2024, **152**, 105647.
21 F. H. A. Zaidi, R. Ahmad, M. M. A. Abdullah, S. Z. Abd Rahim, Z. Yahya, L. Y. Li and R. Ediati, *Constr. Build. Mater.*, 2021, **291**, 123276.
22 U. C. C. S. Siciliano, J. Zhao, A. C. Constâncio Trindade, M. Liebscher, V. Mechtcherine and F. de Andrade Silva, *Constr. Build. Mater.*, 2024, **424**, 135852.
23 J. Yuan, P. He, D. Jia, C. Yang, S. Yan, Z. Yang, X. Duan, S. Wang and Y. Zhou, *Ceram. Int.*, 2016, **42**, 16184–16190.
24 2025/023094 A1, 2025.
25 R. Huang, S. J. Zhang, R. H. Lin and H. J. Jin, *Constr. Build. Mater.*, 2025, **474**, 141135.
26 G. Y. Xiong, X. L. Guo and H. M. Zhang, *Composites, Part B*, 2023, **259**, 110731.
27 W. J. Yan, R. C. Liu, C. Fowler, S. R. Wang and J. J. Qiu, *Comput. Mater. Sci.*, 2024, **237**, 112916.
28 C. J. Gao, R. C. Liu, W. Li, J. J. Qiu and S. R. Wang, *J. Manuf. Process.*, 2023, **89**, 1–9.
29 Z. M. Zhang, C. J. Gao, R. C. Liu, J. J. Qiu, Z. J. Pei and S. R. Wang, *Manuf. Lett.*, 2022, **33**, 640–643.
30 Z. M. Zhang, C. J. Gao, R. C. Liu, W. Li, J. J. Qiu and S. R. Wang, *Addit. Manuf. Lett.*, 2022, **2**, 100030.
31 Z. M. Zhang, R. C. Liu, W. Li, Y. C. Liu, Z. J. Pei, J. J. Qiu and S. R. Wang, *J. Manuf. Process.*, 2021, **71**, 753–762.
32 Z. M. Zhang, R. C. Liu, W. Li, Y. C. Liu, H. C. Luo, L. Zeng, J. J. Qiu and S. R. Wang, *Addit. Manuf.*, 2021, **47**, 102348.
33 B. R. Wang, Z. M. Zhang, Z. J. Pei, J. J. Qiu and S. R. Wang, *Adv. Compos. Hybrid Mater.*, 2020, **3**, 462–472.

34 B. R. Wang, K. F. Arias, Z. M. Zhang, Y. C. Liu, Z. Y. Jiang, H. J. Sue, N. Currie-Gregg, S. Bouslog, Z. J. Pei and S. R. Wang, *Manuf. Lett.*, 2019, **21**, 1–6.
35 J. Sun, W. Liu, S. Chen, G. Qiao and H. Zhang, *Chem. Eng. J.*, 2024, **498**, 155491.
36 S. Alam, T. Manzur, A. Banjara, S. Eklund, A. Radadia, W. Johnston, H. Hashm, J. Williams and J. Matthews, *Constr. Build. Mater.*, 2021, **309**, 125198.
37 B. A. Suslick, J. Hemmer, B. R. Groce, K. J. Stawiasz, P. H. Geubelle, G. Malucelli, A. Mariani, J. S. Moore, J. A. Pojman and N. R. Sottos, *Chem. Rev.*, 2023, **123**, 3237–3298.
38 D. Bistri, A. Cramblitt, I. Arretche, C. Zhang, R. B. Cope, M. Zakoworotny, M. G. Mills, L. E. Rodriguez Koett, L. Chua, R. Gómez-Bombarelli, S. H. Tawfick, N. R. Sottos, J. S. Moore and P. H. Geubelle, *Proc. Natl. Acad. Sci. U. S. A.*, 2025, **122**, e2503176122.
39 S. Wang, X. Ma, L. He, Z. Zhang, L. Li and Y. Li, *Constr. Build. Mater.*, 2019, **198**, 501–511.
40 J. Du, Y. Bu, Z. Shen, X. Hou and C. Huang, *Mater. Des.*, 2016, **109**, 133–145.
41 T. N. Tran, C. Di Mauro, A. Graillot and A. Mija, *Macromolecules*, 2020, **53**, 2526–2538.
42 X. Zhao, Z. Huang, P. Song, H. Chen, H. Yang, L. Xie, X. Liu and Y. Zhang, *Thermochim. Acta*, 2020, **690**, 178657.
43 J. Liu, J.-H. Doh, H. L. Dinh, D. E. L. Ong, G. Zi and I. You, *Constr. Build. Mater.*, 2022, **329**, 127134.
44 M. Upshaw and C. S. Cai, *Case Stud. Constr. Mater.*, 2021, **14**, e00500.
45 X. Zhu and I. G. Richardson, *Cem. Concr. Res.*, 2023, **168**, 107156.
46 E. M. Lloyd, E. C. Feinberg, Y. Gao, S. R. Peterson, B. Soman, J. Hemmer, L. M. Dean, Q. Wu, P. H. Geubelle, N. R. Sottos and J. S. Moore, *ACS Cent. Sci.*, 2021, **7**, 603–612.
47 E. Kapeluszna, Ł. Kotwica, A. Różycka and Ł. Gołek, *Constr. Build. Mater.*, 2017, **155**, 643–653.
48 P. He, M. Wang, S. Fu, D. Jia, S. Yan, J. Yuan, J. Xu, P. Wang and Y. Zhou, *Ceram. Int.*, 2016, **42**, 14416–14422.
49 B. Mailhot, S. Morlat-Thérias, M. Ouahioune and J.-L. Gardette, *Macromol. Chem. Phys.*, 2005, **206**, 575–584.
50 Q. Wang, Z. Min, W. Huang and Z. Shi, *J. Mater. Civ. Eng.*, 2024, **36**, 04024255.
51 C. Galant, B. Fayolle, M. Kuntz and J. Verdu, *Prog. Org. Coat.*, 2010, **69**, 322–329.
52 X. Gu, D. Stanley, W. Byrd, B. Dickens, I. Vaca-Trigo, W. Meeker, N. Tinh, J. Chin and J. Martin, *Service Life Prediction of Polymeric Materials: Global Perspectives*, 2009, pp. 3–28.
53 H. Zheng, Y. Duan, B. Xu, Z. Sun, P. Wang, B. Pang and D. Hou, *Constr. Build. Mater.*, 2025, **485**, 141964.
54 N. F. Ariffin, M. W. Hussin, A. R. Mohd Sam, M. A. R. Bhutta, N. H. A. Khalid and J. Mirza, *Constr. Build. Mater.*, 2015, **94**, 315–322.
55 B. Cheng, J. Yu, T. Arisawa, K. Hayashi, J. J. Richardson, Y. Shibuta and H. Ejima, *Nat. Commun.*, 2022, **13**, 1892.
56 S. L. Yong, D. W. Feng, G. C. Lukey and J. S. J. van Deventer, *Colloids Surf., A*, 2007, **302**, 411–423.
57 H. S. Carslaw, J. Jaeger, L. R. Ingersoll, O. J. Zobel, A. C. Ingersoll and J. Van Vleck, *Phys. Today*, 1948, **1**, 24.